Available online at www.sciencedirect.com
ScienceDirect
Engineering Fracture Mechanics 75 (2008) 1064–1082
Engineering Fracture Mechanics
www.elsevier.com/locate/engfracmech

# Fracture of anodic-bonded silicon-thin film glass-silicon triple stacks

L.Y. Shang, Z.L. Zhang *, B. Skallerud

*Department of Structural Engineering, Norwegian University of Science and Technology (NTNU), Trondheim, Norway*

Received 3 October 2006; received in revised form 3 April 2007; accepted 26 April 2007
Available online 17 May 2007

**Abstract**

In this study we focus on the fracture behavior of two types silicon-thin film glass-silicon (Si-Glass-Si) triple stacks specimens with a sharp corner. We determine the notch stress intensity factor $K^n$ for both specimens using a combination of the Williams eigenfunction expansion method, Stroh's sextic formalism, finite element analysis, and the path-independent H-integral. Empirical solutions of dimensionless stress intensity factors are proposed for two typical specimens, and the dependence of geometry is analyzed. Furthermore, the effect of glass thickness on stress intensity is explored for anodic-bonded Si-Glass-Si triple stacks. We discuss the feasibility of using a critical value of $K^n$ to correlate the failure results for both specimens with various bond area and glass thickness.


*Keywords:* MEMS reliability; Interface fracture; Wafer bonds; Notch mechanics; Path-independent integral

## 1. Introduction

Wafer-to-wafer bonding is critical in the production of micro-electro-mechanical systems (MEMS). Among the different types of wafer bonding, the anodic bonding plays an important role especially for silicon wafers. Anodic bonding (also called field-assisted thermal bonding, electrostatic bonding, etc), a technique for sealing glass and silicon wafers, was presented by Wallis and Pomerantz [1]. The advantage of anodic bonding for MEMS is that the low temperature provides a metalization layer that does not degrade due to temperature effects. Anodic bonding is a commercially available technique. However, thin-film anodic bonding, invented by Brooks and Donovan [2], is not yet industrialized. Si-Glass-Si triple stacks with free edges and corners are also common in wafer-level vacuum packaging of microelectronic devices and microsensors. A thin layer of glass is either electron beam evaporated or sputtered onto a silicon wafer. Another silicon wafer is then bonded onto the glass film. Detailed techniques can be found in Ref. [3]. All published results indicate that a certain minimum critical thickness of the glass layer is required to ensure good bonding, otherwise, it will

* Corresponding author.
*E-mail address:* Zhiliang.zhang@ntnu.no (Z.L. Zhang).

0013-7944/$ - see front matter 
doi:10.1016/j.engfracmech.2007.04.030

**Nomenclature**

| | |
|---|---|
| $a$ | half bond lengths of MESA specimen |
| $\mathbf{a}$, $\mathbf{b}$ | Stroh eigenvectors |
| $b$ | half bond lengths of FRAME specimen |
| $\mathbf{B}$ | matrix |
| $C_{ijk}$ | material elastic stiffness |
| $C_{\alpha\beta}$ | material elastic stiffness with Voigt's notation |
| $\mathbf{D}$ | matrix |
| $E$ | elastic modulus |
| $f_\alpha$ | arbitrary functions with arguments $z_\alpha$ |
| $f_{ij}$ | angular variation of the stress fields |
| $f_1\left(\frac{a}{w}\right)$ | normalized function of $\frac{a}{w}$ for the MESA specimen |
| $f_2\left(\frac{b}{w}\right)$ | normalized function of $\frac{b}{w}$ for the FRAME specimen |
| $g_1\left(\frac{t}{h}\right)$ | normalized function of $\frac{t}{h}$ for the MESA specimen |
| $g_2\left(\frac{t}{h}\right)$ | normalized function of $\frac{t}{h}$ for the FRAME specimen |
| $g_i$ | angular variation of the displacement fields |
| $h$ | the etching depth (the height of bond pad) |
| $K$ | crack stress intensity factor |
| $K^{\mathrm{n}}$ | notch stress intensity factor |
| $K_{\mathrm{C}}$ | critical stress intensity factor |
| $\mathbf{K}$ | stiffness matrix |
| m | deformation mode, m = I, II |
| M | material ID |
| $n_j$ | the unit outward normal to $\Gamma$ |
| $\mathbf{N}_1, \mathbf{N}_2, \mathbf{N}_3$ | matrices in conventional six-dimensional linear eigenvalue problem |
| $p_\alpha$ | eigenvalues ($\alpha = 1,2,\ldots,6$) |
| $q_\alpha$, $h_\alpha$ | complex constants |
| $\mathbf{q}^{\mathrm{M}}$, $\mathbf{h}^{\mathrm{M}}$ | matrix |
| $\mathbf{Q}$, $\mathbf{R}$ and $\mathbf{T}$ | matrices related to material elastic constants |
| $r$, $\theta$ | polar coordinates |
| $t$ | glass thicknesses |
| $t_1$ | thickness of the specimens in $x_3$ direction |
| $\mathbf{t}$ | the traction at any material point $(r, \theta)$ |
| $\mathbf{u}$ | displacement function |
| $w$ | half width of the MESA or FRAME specimen |
| $x_1, x_2, x_3$ | Cartesian coordinates |
| $Y$ | non-dimensional stress intensity factor |
| $Y_{\mathrm{ref}}$ | reference quantity in the empirical solutions due to normalization |
| $Y^m_{\text{H-integral}}$ | non-dimensional stress intensity factor obtained from H-integral approach |
| $Y^m_{u\theta\text{-asymptotic}}$ | non-dimensional stress intensity factor from FEM based on displacements |
| $Y^m_{s\theta\theta-\text{asymptotic}}$ | non-dimensional stress intensity factor from FEM based on opening stress |
| $z_\alpha$ | complex variable $z_\alpha = x_1 + p_\alpha x_2$ |
| $\sigma_{ij}$, $u_i$ | actual stresses and displacements |
| $\sigma^*_{ij}$, $u^*_i$ | complementary stresses and displacements |
| $\sigma_0$ | remote tensile nominal stress |
| $\sigma_{\mathrm{f}}$ | nominal failure strength |
| $\sigma_{\mathrm{N}}$ | net-section failure strength |
| $\delta_{li}$ | Kronecker delta |
| $\lambda - 1$ | stress singularity |

| | |
|---|---|
| $\lambda^*$ | the complementary eigenvalue |
| $\varphi_k$ | stress function components |
| $\boldsymbol{\phi}$ | stress function |
| $\xi_\alpha(\theta)$ | $\xi_\alpha(\theta) = \cos\theta + p_\alpha \sin\theta$ |
| $\boldsymbol{\eta}$ | eigenvectors |
| $\gamma$ | notch angle |
| $\Gamma$ | closed contour around the notch tip |
| $\nu$ | Poisson's ratio |

decrease the bond strength or even result in failure. The minimum thickness of the glass film depends on the concentration of alkali ions in the glass, and the typical minimum thickness is 2 μm [4]. In contrast to sputtering, evaporation can contain many more sodium ions in the glass layer and the anodic bonding can be performed at lower temperature and voltage in the bonding process [5]. An advantage with thin-film anodic bonding, as compared to anodic bonding, is that problems caused by different thermal expansion coefficients and Young's modulus of the glass and the silicon are reduced. Additionally, two highly patterned silicon wafers can be bonded together with thin-film anodic bonding. The disadvantage with the technique is that the process has not been studied and optimized to the same degree as the well known anodic bonding process.

In linear elastic fracture mechanics, the use of a critical stress intensity factor $K_C$ to predict brittle fracture of cracked solids is widely accepted. The feasibility of using the single parameter $K$ (or a function of two parameters in mixed-mode cases) is due to the universal nature of the singular stress field surrounding a crack tip as shown by Williams [6]. In a number of MEMS components, sharp re-entrant corners or notches are introduced, usually to facilitate fabrication. Over the last 20 years, notch mechanics and analysis of an interface between two elastically dissimilar materials have been an active research field. As we know, the near-tip singular stress field in a notched body is characterized by the form $\sigma_{ij} = K_{\mathrm{I}}^{\mathrm{n}} r^{\lambda_{\mathrm{I}}-1} f_{ij}^{\mathrm{I}}(\theta) + K_{\mathrm{II}}^{\mathrm{n}} r^{\lambda_{\mathrm{II}}-1} f_{ij}^{\mathrm{II}}(\theta)$. The stress singularity $\lambda - 1$ for various single and multiple-phase notch geometries in both isotropic [7–12] and anisotropic [13–20] media has been studied. For multimaterial media, the situation becomes complicated as in mixed-mode deformation the asymptotic elastic fields depend on radial position, elastic mismatch and interface corner geometry. Accordingly, the mode I and mode II fields are usually not symmetric with the notch bisector as they are for the isotropic homogeneous case. An efficient computational procedure to obtain stress intensity factors around multimaterial interface corners can be realized by the path-independent H-integral. The interested readers can confer the review of Hutchinson and Suo [21], and Labossiere and Dunn [22] for more details. Despite some extensive studies related to anisotropic materials and bimaterial media, few studies focused on the three-material interface notch problems. This gives motivation of our work.

In this paper, we extend the H-integral approach to compute stress intensity factors at interface corners of thin-film anodic-bonded Si-Glass-Si triple stacks. Two types of specimens, named MESA and FRAME, with different bond area and various glass thickness are considered. We apply this approach to the mixed-mode I and II loading. The stress intensity factors obtained from the H-integral approach are in good agreement with those obtained by matching the asymptotic solutions with detailed finite element analysis. Empirical solutions of dimensionless stress intensity factors are established to facilitate engineering application. Furthermore, the effect of glass thickness on the stress intensity is studied for triple stacks. The magnitude of critical stress intensity factor for thin-film Si-Glass-Si triple stacks is determined from tests. Finally, mesh effect and some uncertainties are discussed.

## 2. Asymptotic analysis of interface notch tip fields with anisotropic elastic materials

The asymptotic analysis of anisotropic elastic fields at the bimaterial interface corner is briefly presented. The asymptotic analysis solves two eigenvalue problems obtained by Stroh's sextic formalism [22–24] and the eigenfunction expansion method of Williams [6].

### 2.1. First eigenvalue problem – Stroh's sextic formalism

According to Stroh, when two-dimensional deformations depend only on $x_1$ and $x_2$, the displacement $\mathbf{u}$ and stress function $\boldsymbol{\phi}$ of an anisotropic elastic solid in a fixed rectangular coordinate system can be generally expressed as

$$\mathbf{u} = \sum_{\alpha=1}^{3}[\mathbf{a}_\alpha f_\alpha(z_\alpha) + \bar{\mathbf{a}}_\alpha f_{\alpha+3}(\bar{z}_\alpha)] \tag{2.1}$$

$$\boldsymbol{\phi} = \sum_{\alpha=1}^{3}[\mathbf{b}_\alpha f_\alpha(z_\alpha) + \bar{\mathbf{b}}_\alpha f_{\alpha+3}(\bar{z}_\alpha)] \tag{2.2}$$

Here $f_\alpha$ are arbitrary functions of their arguments $z_\alpha$ depending on the geometry and loading, $z_\alpha = x_1 + p_\alpha x_2$ is the complex variable. The six complex eigenvalues $p_\alpha$ satisfy $p_{\alpha+3} = \bar{p}_\alpha$ and are the solutions of the quadratic eigenvalue problem (2.4). In addition, $\mathbf{a}$ and $\mathbf{b}$ are the Stroh eigenvectors and satisfy $\mathbf{a}_{\alpha+3} = \bar{\mathbf{a}}_\alpha$ and $\mathbf{b}_{\alpha+3} = \bar{\mathbf{b}}_\alpha$ related through the matrix $\mathbf{Q}$, $\mathbf{R}$ and $\mathbf{T}$ described later. $p_\alpha$, $\mathbf{a}_\alpha$ and $\mathbf{b}_\alpha$ depend only on the elastic stiffnesses $C_{ijkl}$. Without loss of generality, the imaginary part of $p_\alpha$ is taken to be positive. Overbar of $p$, $z$, $\mathbf{a}$, $\mathbf{b}$ denotes the complex conjugate.

In terms of the stress–strain laws $\sigma_{ij} = C_{ijkl}u_{k,l}$ and using Eq. (2.1), the equilibrium equations $C_{ijkl}u_{k,lj} = 0$ can be written

$$C_{ijkl}(\delta_{l1} + \delta_{l2}p)(\delta_{j1} + \delta_{j2}p)a_k = 0 \tag{2.3}$$

in which a comma denotes differentiation and $\delta_{li}$ is the Kronecker delta. The above equation can be written in matrix form as

$$\{\mathbf{Q} + p(\mathbf{R} + \mathbf{R}^{\mathrm{T}}) + p^2\mathbf{T}\}\mathbf{a} = \mathbf{0} \tag{2.4}$$

where $Q_{ik} = C_{i1k1}$, $R_{ik} = C_{i1k2}$ and $T_{ik} = C_{i2k2}$. For a non-trivial solution of $\mathbf{a}$, we must have $\det|\mathbf{Q} + p(\mathbf{R} + \mathbf{R}^{\mathrm{T}}) + p^2\mathbf{T}| = 0$, which results in six roots for the eigenvalue $p$. In matrix forms and with Voigt's notation

$$\mathbf{Q} = \begin{bmatrix} C_{11} & C_{16} & C_{15} \\ C_{16} & C_{66} & C_{56} \\ C_{15} & C_{56} & C_{55} \end{bmatrix}, \quad \mathbf{T} = \begin{bmatrix} C_{66} & C_{26} & C_{46} \\ C_{26} & C_{22} & C_{24} \\ C_{46} & C_{24} & C_{44} \end{bmatrix} \quad \text{and} \quad \mathbf{R} = \begin{bmatrix} C_{16} & C_{12} & C_{14} \\ C_{66} & C_{26} & C_{46} \\ C_{56} & C_{25} & C_{45} \end{bmatrix} \tag{2.5}$$

$$\begin{bmatrix} C_{11} + 2pC_{16} + p^2C_{66} & C_{16} + p(C_{12} + C_{66}) + p^2C_{26} & C_{15} + p(C_{14} + C_{56}) + p^2C_{46} \\ & C_{66} + 2pC_{26} + p^2C_{22} & C_{56} + p(C_{46} + C_{25}) + p^2C_{24} \\ \text{symmetric} & & C_{55} + 2pC_{45} + p^2C_{44} \end{bmatrix}\mathbf{a} = \mathbf{0} \tag{2.6}$$

Differentiating Eq. (2.1) and then inserting into constitutive equation, we can obtain $\sigma_{ij}$

$$\begin{aligned} \sigma_{i1} &= (Q_{ik} + pR_{ik})a_k f'(z) \\ \sigma_{i2} &= (R_{ki} + pT_{ik})a_k f'(z) \end{aligned} \tag{2.7}$$

in which the prime denotes differentiation with the argument $z$. Making use of Eq. (2.2), the relation between $\mathbf{a}$ and $\mathbf{b}$ can be written

$$\mathbf{b} = (\mathbf{R}^{\mathrm{T}} + p\mathbf{T})\mathbf{a} = -\frac{1}{p}(\mathbf{Q} + p\mathbf{R})\mathbf{a} \tag{2.8}$$

The above quadratic eigenvalue problem (three dimensional) can be recast as a conventional six-dimensional linear eigenvalue problem

$$\begin{aligned} &\begin{bmatrix} \mathbf{N}_1 & \mathbf{N}_2 \\ \mathbf{N}_3 & \mathbf{N}_1^T \end{bmatrix}\begin{Bmatrix} \mathbf{a} \\ \mathbf{b} \end{Bmatrix} = p\begin{Bmatrix} \mathbf{a} \\ \mathbf{b} \end{Bmatrix} \\ &\Rightarrow \mathbf{N}\boldsymbol{\eta} = p\boldsymbol{\eta}, \quad \boldsymbol{\eta} = \begin{Bmatrix} \mathbf{a} \\ \mathbf{b} \end{Bmatrix} \end{aligned} \tag{2.9}$$

where $\mathbf{N}_1 = -\mathbf{T}^{-1}\mathbf{R}^{\mathrm{T}}$, $\mathbf{N}_2 = \mathbf{T}^{-1}$ and $\mathbf{N}_3 = -\mathbf{Q} + \mathbf{R}\mathbf{T}^{-1}\mathbf{R}^{\mathrm{T}}$. Since $p$ cannot be real if the strain energy is to be positive [25], we have three pairs of complex conjugates for $p$ as well as for $\eta$. If $p_\alpha$ and $\eta_\alpha(\alpha = 1,2,\ldots,6)$ are the eigenvalues and eigenvectors, we let

$$\left.\begin{aligned} p_{\alpha+3} &= \bar{p}_\alpha, \quad \mathrm{Im}p_\alpha > 0 \\ \eta_{\alpha+3} &= \bar{\eta}_\alpha \end{aligned}\right\} \alpha = 1,2,3 \tag{2.10}$$

where Im denotes the imaginary part.

The Stroh eigenvectors are determined up to an arbitrary constant. They are normalized as

$$\mathbf{a}_\alpha = \frac{\hat{\mathbf{a}}_\alpha}{\sqrt{2\hat{\mathbf{a}}_\alpha^{\mathrm{T}}\hat{\mathbf{b}}_\alpha}} \quad \text{and} \quad \mathbf{b}_\alpha = \frac{\hat{\mathbf{b}}_\alpha}{\sqrt{2\hat{\mathbf{a}}_\alpha^{\mathrm{T}}\hat{\mathbf{b}}_\alpha}} \tag{2.11}$$

where $\hat{\mathbf{a}}_\alpha$ and $\hat{\mathbf{b}}_\alpha$ are the non-normalized eigenvectors, i.e. those that would be produced by a standard eigensolver; $\mathbf{a}_\alpha$ and $\mathbf{b}_\alpha$ represent the direction of the displacement $\mathbf{u}_\alpha$ and traction $\mathbf{t}_\alpha$, respectively.

### 2.2. Second eigenvalue problem – notch tip stress singularity

A stress singularity exists at sharp notches/crack tips. The degree of stress singularity is obtained from solving the second eigenvalue problem.

The traction $\mathbf{t}$ at any material point $(r,\theta)$ along the radial line from the notch tip can be written

$$\mathbf{t} = \frac{\mathrm{d}}{\mathrm{d}r}\boldsymbol{\phi} \quad \text{or} \quad \sigma_{k1} = -\frac{\partial\varphi_k}{\partial x_2}, \quad \sigma_{k2} = \frac{\partial\varphi_k}{\partial x_1} \tag{2.12}$$

where $\boldsymbol{\phi}$ is the stress function given by Eq. (2.2) and $r$ is the radial distance measured from the notch tip.

By choosing $f(z_\alpha)$ [19,22,24] as

$$f_\alpha(z_\alpha) = \frac{1}{\lambda}z_\alpha^\lambda q_\alpha \quad \text{and} \quad f_{\alpha+3}(\bar{z}_\alpha) = \frac{1}{\lambda}\bar{z}_\alpha^\lambda h_\alpha \tag{2.13}$$

where $q_\alpha$ and $h_\alpha$ are the unknown complex constants and will be determined by Eq. (2.19) once $\lambda$ is obtained. Using the expression $z_\alpha = x_1 + p_\alpha x_2 = r\xi_\alpha(\theta) = r(\cos\theta + p_\alpha\sin\theta)$, the displacement and traction functions can be written

$$\begin{aligned} \mathbf{u}^{\mathrm{M}} &= \frac{1}{\lambda}r^\lambda\sum_{\alpha=1}^{3}\left[\xi_\alpha^{\mathrm{M}}(\theta)^\lambda\mathbf{a}_\alpha q_\alpha + \bar{\xi}_\alpha^{\mathrm{M}}(\theta)^\lambda\bar{\mathbf{a}}_\alpha h_\alpha\right] \\ \mathbf{t}^{\mathrm{M}} &= \frac{\lambda}{r}\boldsymbol{\phi} = r^{\lambda-1}\sum_{\alpha=1}^{3}\left[\xi_\alpha^{\mathrm{M}}(\theta)^\lambda\mathbf{b}_\alpha q_\alpha + \bar{\xi}_\alpha^{\mathrm{M}}(\theta)^\lambda\bar{\mathbf{b}}_\alpha h_\alpha\right] \end{aligned} \tag{2.14}$$

where superscript M indicates material A or B. The second eigenvalue problem can be solved by using the boundary conditions for the interface notch problem, see Fig. 1. There are four sets of boundary conditions:

$$\begin{aligned} &\mathbf{t}^{\mathrm{A}}(\alpha) = 0, \quad \sum_{\alpha=1}^{3}\xi_\alpha^{\mathrm{A}}(\alpha)^\lambda\mathbf{b}_\alpha^{\mathrm{A}}q_\alpha^{\mathrm{A}} + \sum_{\alpha=1}^{3}\bar{\xi}_\alpha^{\mathrm{A}}(\alpha)^\lambda\bar{\mathbf{b}}_\alpha^{\mathrm{A}}h_\alpha^{\mathrm{A}} = 0 \\ &\mathbf{t}^{\mathrm{B}}(-\beta) = 0, \quad \sum_{\alpha=1}^{3}\xi_\alpha^{\mathrm{B}}(-\beta)^\lambda\mathbf{b}_\alpha^{\mathrm{B}}q_\alpha^{\mathrm{B}} + \sum_{\alpha=1}^{3}\bar{\xi}_\alpha^{\mathrm{B}}(-\beta)^\lambda\bar{\mathbf{b}}_\alpha^{\mathrm{B}}h_\alpha^{\mathrm{B}} = 0 \\ &\mathbf{t}^{\mathrm{A}}(0) = \mathbf{t}^{\mathrm{B}}(0), \quad \sum_{\alpha=1}^{3}\xi_\alpha^{\mathrm{A}}(0)^\lambda\mathbf{b}_\alpha^{\mathrm{A}}q_\alpha^{\mathrm{A}} + \sum_{\alpha=1}^{3}\bar{\xi}_\alpha^{\mathrm{A}}(0)^\lambda\bar{\mathbf{b}}_\alpha^{\mathrm{A}}h_\alpha^{\mathrm{A}} - \sum_{\alpha=1}^{3}\xi_\alpha^{\mathrm{B}}(0)^\lambda\mathbf{b}_\alpha^{\mathrm{B}}q_\alpha^{\mathrm{B}} - \sum_{\alpha=1}^{3}\bar{\xi}_\alpha^{\mathrm{B}}(0)^\lambda\bar{\mathbf{b}}_\alpha^{\mathrm{B}}h_\alpha^{\mathrm{B}} = 0 \\ &\mathbf{u}^{\mathrm{A}}(0) = \mathbf{u}^{\mathrm{B}}(0), \quad \sum_{\alpha=1}^{3}\xi_\alpha^{\mathrm{A}}(0)^\lambda\mathbf{a}_\alpha^{\mathrm{A}}q_\alpha^{\mathrm{A}} + \sum_{\alpha=1}^{3}\bar{\xi}_\alpha^{\mathrm{A}}(0)^\lambda\bar{\mathbf{a}}_\alpha^{\mathrm{A}}h_\alpha^{\mathrm{A}} - \sum_{\alpha=1}^{3}\xi_\alpha^{\mathrm{B}}(0)^\lambda\mathbf{a}_\alpha^{\mathrm{B}}q_\alpha^{\mathrm{B}} - \sum_{\alpha=1}^{3}\bar{\xi}_\alpha^{\mathrm{B}}(0)^\lambda\bar{\mathbf{a}}_\alpha^{\mathrm{B}}h_\alpha^{\mathrm{B}} = 0 \end{aligned} \tag{2.15}$$

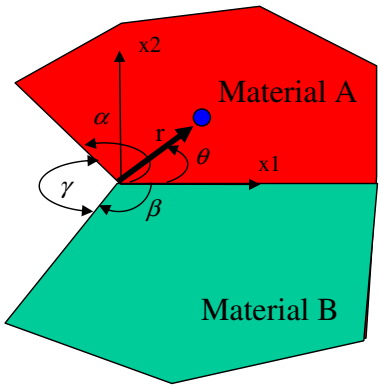


Fig. 1. Configuration of bimaterial interface corner.

The equations above can be rewritten as

$$\begin{aligned}
&\mathbf{B}^{A}\mathbf{q}^{A} + \bar{\mathbf{B}}^{A}\mathbf{h}^{A} = \mathbf{0}\\
&\mathbf{B}^{B}\mathbf{q}^{B} + \bar{\mathbf{B}}^{B}\mathbf{h}^{B} = \mathbf{0}\\
&\mathbf{b}^{A}\mathbf{q}^{A} + \bar{\mathbf{b}}^{A}\mathbf{h}^{A} - \mathbf{b}^{B}\mathbf{q}^{B} - \bar{\mathbf{b}}^{B}\mathbf{h}^{B} = \mathbf{0}\\
&\mathbf{a}^{A}\mathbf{q}^{A} + \bar{\mathbf{a}}^{A}\mathbf{h}^{A} - \mathbf{a}^{B}\mathbf{q}^{B} - \bar{\mathbf{a}}^{B}\mathbf{h}^{B} = \mathbf{0}
\end{aligned} \tag{2.16}$$

where

$$\begin{aligned}
&\mathbf{B}^{A} = \left[\,\xi_1^{A}(\alpha)^{\lambda}\mathbf{b}_1^{A},\quad \xi_2^{A}(\alpha)^{\lambda}\mathbf{b}_2^{A},\quad \xi_3^{A}(\alpha)^{\lambda}\mathbf{b}_3^{A}\,\right],\quad \mathbf{B}^{B} = \left[\,\xi_1^{B}(-\beta)^{\lambda}\mathbf{b}_1^{B},\quad \xi_2^{B}(-\beta)^{\lambda}\mathbf{b}_2^{B},\quad \xi_3^{B}(-\beta)^{\lambda}\mathbf{b}_3^{B}\,\right],\\
&\mathbf{a}^{M} = \left[\mathbf{a}_1^{M}, \mathbf{a}_2^{M}, \mathbf{a}_3^{M}\right],\quad \mathbf{b}^{M} = [\mathbf{b}_1^{M}, \mathbf{b}_2^{M}, \mathbf{b}_3^{M}],\quad \mathbf{q}^{M} = [q_1^{M}, q_2^{M}, q_3^{M}]^{T},\quad \mathbf{h}^{M} = [h_1^{M}, h_2^{M}, h_3^{M}]^{T}\\
&(M = A, B)
\end{aligned}$$

From the first two equations, we have

$$\begin{aligned}
&\mathbf{h}^{A} = -(\overline{\mathbf{B}}^{A})^{-1}\mathbf{B}^{A}\mathbf{q}^{A}\\
&\mathbf{q}^{B} = -(\mathbf{B}^{B})^{-1}\overline{\mathbf{B}}^{B}\mathbf{h}^{B}
\end{aligned} \tag{2.17}$$

By substituting Eq. (2.17) into the last two equations of Eq. (2.16), we get

$$\begin{bmatrix} \mathbf{b}^{A}(\mathbf{B}^{A})^{-1} - \bar{\mathbf{b}}^{A}(\overline{\mathbf{B}}^{A})^{-1} & (\mathbf{b}^{B}(\mathbf{B}^{B})^{-1} - \bar{\mathbf{b}}^{B}(\overline{\mathbf{B}}^{B})^{-1}) \\ \mathbf{a}^{A}(\mathbf{B}^{A})^{-1} - \bar{\mathbf{a}}^{A}(\overline{\mathbf{B}}^{A})^{-1} & (\mathbf{a}^{B}(\mathbf{B}^{B})^{-1} - \bar{\mathbf{a}}^{B}(\overline{\mathbf{B}}^{B})^{-1}) \end{bmatrix} \begin{Bmatrix} \mathbf{B}^{A}\mathbf{q}^{A} \\ \overline{\mathbf{B}}^{B}\mathbf{h}^{B} \end{Bmatrix} = 0 \tag{2.18}$$

that results in 6 simultaneous eigenvalue equations

$$\mathbf{K}(\lambda)\mathbf{D} = 0 \tag{2.19}$$

where $\mathbf{D} = [\mathbf{B}^{A}\mathbf{q}^{A},\ \overline{\mathbf{B}}^{B}\mathbf{h}^{B}]^{T}$. For the single crystal silicon and glass material considered in this study, $\mathbf{K}$, can be partitioned into inplane and antiplane deformations.

$$\mathbf{K} = \begin{bmatrix} \mathbf{K}_{IP} & \mathbf{0} \\ \mathbf{0} & \mathbf{K}_{AP} \end{bmatrix} \tag{2.20}$$

In order to obtain a non-trivial solution, we get the characteristic equation for $\lambda$

$$\det[\mathbf{K}(\lambda)] = 0 \tag{2.21}$$

## 3. H-integral approach

A path-independent H-integral approach for calculation of the stress intensity factor at sharp notches is briefly presented here. The main advantage of this method is that the stress intensity factor can be obtained by a contour integral around the notch tip with only tractions and displacements required.

Considering the configuration of a bimaterial interface corner shown in Fig. 1, the upper and lower notch faces are at $\theta = \alpha$ and $\theta = -\beta$ and the notch angle is $\gamma$, where angle $\theta$ is measured from the interface. For anisotropic materials, their elastic stiffnesses can be transformed with respect to the $x_1 - x_2$ axes [26]. The notch faces are traction-free and the notched body is loaded at remote boundaries by tractions or displacements.

In this paper we study only the inplane fields and real eigenvalues $\lambda_{\mathrm{I}}$ and $\lambda_{\mathrm{II}}$ solved by (2.21). With normalizations of the mode I fields by $\sigma_{22}(\theta = 0) = K_{\mathrm{I}}^{\mathrm{n}} r^{\lambda_{\mathrm{I}}-1}$ and of the mode II fields by $\sigma_{12}(\theta = 0) = K_{\mathrm{II}}^{\mathrm{n}} r^{\lambda_{\mathrm{II}}-1}$, the inplane asymptotic singular fields near the notch tip can be expressed as

$$\begin{aligned} \sigma_{ij}^{\mathrm{M}}(r,\theta) &= K_{\mathrm{I}}^{\mathrm{n}} r^{\lambda_{\mathrm{I}}-1} f_{ij}^{\mathrm{IM}}(\theta) + K_{\mathrm{II}}^{\mathrm{n}} r^{\lambda_{\mathrm{II}}-1} f_{ij}^{\mathrm{IIM}}(\theta) \\ u_i^{\mathrm{M}}(r,\theta) &= K_{\mathrm{I}}^{\mathrm{n}} r^{\lambda_{\mathrm{I}}} g_i^{\mathrm{IM}}(\theta) + K_{\mathrm{II}}^{\mathrm{n}} r^{\lambda_{\mathrm{II}}} g_i^{\mathrm{IIM}}(\theta) \end{aligned} \tag{3.1}$$

and before normalization

$$\begin{aligned} f_{i1}^{\mathrm{IM}}(\theta) &= -\sum_{\alpha=1}^{2}\left[p_\alpha^{\mathrm{M}}\left(\mathbf{b}_\alpha^{\mathrm{M}}\right)_i \xi_\alpha^{\mathrm{M}}(\theta)^{\lambda_{\mathrm{I}}-1} q_\alpha^{\mathrm{IM}} + p_{\alpha+3}^{\mathrm{M}}\left(\mathbf{b}_{\alpha+3}^{\mathrm{M}}\right)_i \xi_{\alpha+3}^{\mathrm{M}}(\theta)^{\lambda_{\mathrm{I}}-1} h_\alpha^{\mathrm{IM}}\right] \\ f_{i2}^{\mathrm{IM}}(\theta) &= \sum_{\alpha=1}^{2}\left[\left(\mathbf{b}_\alpha^{\mathrm{M}}\right)_i \xi_\alpha^{\mathrm{M}}(\theta)^{\lambda_{\mathrm{I}}-1} q_\alpha^{\mathrm{IM}} + \left(\mathbf{b}_{\alpha+3}^{\mathrm{M}}\right)_i \xi_{\alpha+3}^{\mathrm{M}}(\theta)^{\lambda_{\mathrm{I}}-1} h_\alpha^{\mathrm{IM}}\right] \\ g_i^{\mathrm{IM}}(\theta) &= \frac{1}{\lambda_{\mathrm{I}}}\sum_{\alpha=1}^{2}\left[\left(\mathbf{a}_\alpha^{\mathrm{M}}\right)_i \xi_\alpha^{\mathrm{M}}(\theta)^{\lambda_{\mathrm{I}}} q_\alpha^{\mathrm{IM}} + \left(\mathbf{a}_{\alpha+3}^{\mathrm{M}}\right)_i \xi_{\alpha+3}^{\mathrm{M}}(\theta)^{\lambda_{\mathrm{I}}} h_\alpha^{\mathrm{IM}}\right] \\ f_{i1}^{\mathrm{IIM}}(\theta) &= -\sum_{\alpha=1}^{2}\left[p_\alpha^{\mathrm{M}}\left(\mathbf{b}_\alpha^{\mathrm{M}}\right)_i \xi_\alpha^{\mathrm{M}}(\theta)^{\lambda_{\mathrm{II}}-1} q_\alpha^{\mathrm{IIM}} + p_{\alpha+3}^{\mathrm{M}}\left(\mathbf{b}_{\alpha+3}^{\mathrm{M}}\right)_i \xi_{\alpha+3}^{\mathrm{M}}(\theta)^{\lambda_{\mathrm{II}}-1} h_\alpha^{\mathrm{IIM}}\right] \\ f_{i2}^{\mathrm{IIM}}(\theta) &= \sum_{\alpha=1}^{2}\left[\left(\mathbf{b}_\alpha^{\mathrm{M}}\right)_i \xi_\alpha^{\mathrm{M}}(\theta)^{\lambda_{\mathrm{II}}-1} q_\alpha^{\mathrm{IIM}} + \left(\mathbf{b}_{\alpha+3}^{\mathrm{M}}\right)_i \xi_{\alpha+3}^{\mathrm{M}}(\theta)^{\lambda_{\mathrm{II}}-1} h_\alpha^{\mathrm{IIM}}\right] \\ g_i^{\mathrm{IIM}}(\theta) &= \frac{1}{\lambda_{\mathrm{II}}}\sum_{\alpha=1}^{2}\left[\left(\mathbf{a}_\alpha^{\mathrm{M}}\right)_i \xi_\alpha^{\mathrm{M}}(\theta)^{\lambda_{\mathrm{II}}} q_\alpha^{\mathrm{IIM}} + \left(\mathbf{a}_{\alpha+3}^{\mathrm{M}}\right)_i \xi_{\alpha+3}^{\mathrm{M}}(\theta)^{\lambda_{\mathrm{II}}} h_\alpha^{\mathrm{IIM}}\right] \end{aligned} \tag{3.2}$$

Here the superscript M indicates material A or B, $K_{\mathrm{m}}^{\mathrm{n}}$ are notch stress intensity factors where m corresponds to deformation mode I or II that are analogous to the opening and sliding modes in a homogeneous notched solid, $\lambda_{\mathrm{n}} - 1$ are the stress singularities, and $f_{ij}^{\mathrm{mM}}$ and $g_i^{\mathrm{mM}}$ are functions depending on angle $\theta$ and material stiffnesses. In Eq. (3.1), only the stress intensity factors $K_{\mathrm{I}}^{\mathrm{n}}$ and $K_{\mathrm{II}}^{\mathrm{n}}$ cannot be determined from the asymptotic analysis. They depend on the geometry of the notched body, material elastic constants, and the far-field loading.

The path independent H-integral is based on the application of Betti's reciprocal work theorem which suppose two sets of elastic fields: the actual and the complementary. If $\lambda$ is a root of Eq. (2.21), so is $\lambda^* = -\lambda$ [27]. Hence, the chosen complementary solution is given by Eqs. (3.3) and (3.4).

$$\begin{aligned} f_\alpha^*(z_\alpha) &= \tfrac{1}{\lambda^*} z_\alpha^{\lambda^*} q_\alpha^* \\ f_{\alpha+3}^*(\bar{z}_\alpha) &= \tfrac{1}{\lambda^*} \bar{z}_\alpha^{\lambda^*} h_\alpha^* \end{aligned} \tag{3.3}$$

$$\begin{aligned} \sigma_{ij}^{\mathrm{M}^*}(r,\theta) &= K_{\mathrm{I}}^{\mathrm{n}^*} r^{-\lambda_{\mathrm{I}}-1} f_{ij}^{-\mathrm{IM}^*}(\theta) + K_{\mathrm{II}}^{\mathrm{n}^*} r^{-\lambda_{\mathrm{II}}-1} f_{ij}^{\mathrm{IIM}^*}(\theta) \\ u_i^{\mathrm{M}^*}(r,\theta) &= K_{\mathrm{I}}^{\mathrm{n}^*} r^{-\lambda_{\mathrm{I}}} g_i^{\mathrm{IM}^*}(\theta) + K_{\mathrm{II}}^{\mathrm{n}^*} r^{-\lambda_{\mathrm{II}}} g_i^{\mathrm{IIM}^*}(\theta) \end{aligned} \tag{3.4}$$

In the absence of body forces and singularities, the H-integral takes the form:

$$H = \int_{\Gamma} \left( \sigma_{ij} u_i^* - \sigma_{ij}^* u_i \right) n_j \, \mathrm{d}s = 0 \tag{3.5}$$

where $\Gamma$ is a closed contour around the notch tip, $n_j$ is the unit outward normal to $\Gamma$, $\sigma_{ij}$, $u_i$ and $\sigma_{ij}^*$, $u_i^*$ are the actual and complementary stresses and displacements that satisfy the equilibrium and constitutive relations, respectively.

Taking a counter-clockwise contour around the notch tip from the lower face to upper face, in polar coordinates, the above equation is expressed as

$$H = \int_{-\beta}^{\alpha} \left( \sigma_{rr} u_r^* + \sigma_{r\theta} u_\theta^* - \sigma_{rr}^* u_r - \sigma_{r\theta}^* u_\theta \right) r \, \mathrm{d}\theta \tag{3.6}$$

and in Cartesian coordinates, it is given by

$$H = \int_{y} \left( \sigma_x u_x^* + \sigma_{xy} u_y^* - \sigma_x^* u_x - \sigma_{xy}^* u_y \right) \mathrm{d}y + \int_{x} \left( \sigma_y u_y^* + \sigma_{xy} u_x^* - \sigma_y^* u_y - \sigma_{xy}^* u_x \right) \mathrm{d}x \tag{3.7}$$

Taking advantage of Eq. (3.5), we obtain an explicit expression for the mode I scaling factor $K_{\mathrm{I}}^{\mathrm{n}^*}$ by setting $H = H_{\mathrm{I}} = K_{\mathrm{I}}^{\mathrm{n}}$ and similarly the mode II scaling factor $K_{\mathrm{II}}^{\mathrm{n}^*}$ by setting $H = H_{\mathrm{II}} = K_{\mathrm{II}}^{\mathrm{n}}$.

Dimensionless considerations illustrate that the stress intensity factor $K^{\mathrm{n}}$ takes the form:

$$K^{\mathrm{n}} = \sigma_0 (\text{length})^{1-\lambda} Y(\text{geometry}) \tag{3.8}$$

where $\sigma_0$ is a nominal stress and $Y$ is a non-dimensional function of geometry.

## 4. Application to Si-Glass-Si triple stacks

### *4.1. Specification of Si-Glass-Si triple stacks with mixed-mode I and II loading*

In this work, triple stacks are composed of Si-Glass-Si multimaterials. Two types of specimens, MESA and FRAME, Fig. 2, have been studied. The overall width of the specimen ($2w$) is 3500 μm, the etching depth (the height of bond pad, $h$) is 18 μm. Five bond lengths ($2a$), 700, 1000, 1414, 1700 and 2000 μm, and four glass thicknesses ($t$), 3, 3.6, 5 and 10 μm, have been considered for the MESA specimens. For the FRAME specimens, five bond lengths ($2b$), 400, 800, 1200, 1600 and 1900 μm, and five glass thicknesses, 3, 3.6, 5, 10 and 18 μm, have been analyzed. A remote tensile nominal stress $\sigma_0 = F/2wt_1$ is applied to all the specimens, where $t_1$ is the thickness of the specimen in $x_3$ direction. Brittle fracture initiated at the interface corner. It should be

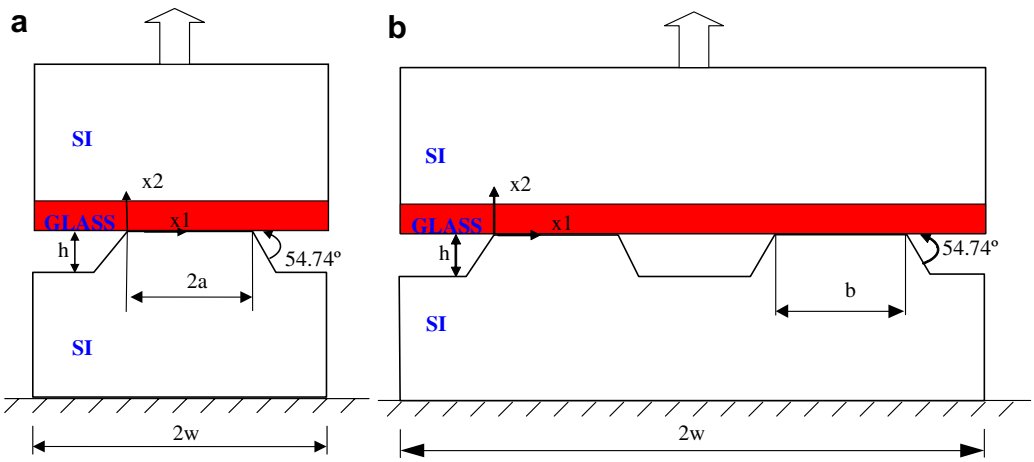


Fig. 2. 54.74° Notched (a) MESA and (b) FRAME triple-stacks specimens.

noted that even though the specimens have remote tension, they are subjected to mixed-mode I and II loading at notch tip. The interface corner is $\gamma = 54.74°$ which is a result of etching process. Silicon is an elastic brittle material and its elastic stiffness matrix corresponding to the $x_1 - x_2$ axes in Fig. 2 is given by Eq. (4.1). Corning #7740 PYREX glass is used here with elastic modulus $E = 63$ GPa and Poisson's ratio $v = 0.2$. Making use of symmetry, we only take account of a half-model in the plane strain finite element analysis for both specimens. ABAQUS was used in the analysis.

$$C_{ij} = \begin{bmatrix} 194.36 & 63.9 & 35.24 & 0 & 0 & 0 \\ 63.9 & 165.7 & 63.9 & 0 & 0 & 0 \\ 35.24 & 63.9 & 194.36 & 0 & 0 & 0 \\ 0 & 0 & 0 & 79.56 & 0 & 0 \\ 0 & 0 & 0 & 0 & 50.9 & 0 \\ 0 & 0 & 0 & 0 & 0 & 79.56 \end{bmatrix} \text{GPa} \tag{4.1}$$

For the materials considered, using the asymptotic singularity analysis described in Section 2, we obtain the eigenvalues $\lambda_{\mathrm{I}} = 0.5078$, $\lambda_{\mathrm{II}} = 0.6199$. The angular variation of the stress and displacement fields $f_{ij}^{\mathrm{I}}(\theta)$, $g_i^{\mathrm{I}}(\theta)$, $f_{ij}^{\mathrm{I}^*}(\theta)$ and $g_i^{\mathrm{I}^*}(\theta)$ are shown in Fig. 3a, and $f_{ij}^{\mathrm{II}}(\theta)$, $g_i^{\mathrm{II}}(\theta)$, $f_{ij}^{\mathrm{II}^*}(\theta)$ and $g_i^{\mathrm{II}^*}(\theta)$ are shown in Fig. 3b where $i,j = r,\theta$.

In order to study the effect of glass thickness and bond area on the fracture behavior, dimensional considerations of $K_{\mathrm{m}}^{\mathrm{n}}$ yield the following form:

$$K_{\mathrm{m}}^{\mathrm{n}} = \sigma_0 w^{1-\lambda_{\mathrm{m}}} Y_{\mathrm{m}}^{\mathrm{n}}\left(\frac{a}{w}, \frac{h}{w}, \frac{t}{h}\right) \tag{4.2}$$

where $Y_{\mathrm{m}}^{\mathrm{n}}\left(\frac{a}{w}, \frac{h}{w}, \frac{t}{h}\right)(\mathrm{m} = \mathrm{I}, \mathrm{II})$ is a dimensionless calibration function and is specific for the geometry, the thickness of glass layer, boundary conditions, and elastic constants. In this study, we only take a fixed value of $\frac{h}{w} = 0.0103$; consequently, $Y_{\mathrm{m}}^{\mathrm{n}}\left(\frac{a}{w}, \frac{h}{w}, \frac{t}{h}\right)$ reduces to $Y_{\mathrm{m}}^{\mathrm{n}}\left(\frac{a}{w}, \frac{t}{h}\right)$. Furthermore, we can write

$$\begin{aligned} Y_{\mathrm{m}}^{\mathrm{n}}\left(\frac{a}{w}, \frac{t}{h}\right) &= Y_{\mathrm{ref1}} \cdot f_1\left(\frac{a}{w}\right) \cdot g_1\left(\frac{t}{h}\right) \quad \text{for MESA} \\ Y_{\mathrm{m}}^{\mathrm{n}}\left(\frac{b}{w}, \frac{t}{h}\right) &= Y_{\mathrm{ref2}} \cdot f_2\left(\frac{b}{w}\right) \cdot g_2\left(\frac{t}{h}\right) \quad \text{for FRAME} \end{aligned} \tag{4.3}$$

where

$$f_1\left(\frac{a}{w}\right) = \frac{Y_{\mathrm{m}}^{\mathrm{n}}\left(\frac{a}{w}, \frac{t}{h} = 0.2\right)}{Y_{\mathrm{ref1}}}, \quad g_1\left(\frac{t}{h}\right) = \frac{Y_{\mathrm{m}}^{\mathrm{n}}\left(\frac{a}{w} = 0.286, \frac{t}{h}\right)}{Y_{\mathrm{ref1}}}, \quad Y_{\mathrm{ref1}} = Y_{\mathrm{m}}^{\mathrm{n}}\left(\frac{a}{w} = 0.286, \frac{t}{h} = 0.2\right)$$

$$f_2\left(\frac{b}{w}\right) = \frac{Y_{\mathrm{m}}^{\mathrm{n}}\left(\frac{b}{w}, \frac{t}{h} = 0.2\right)}{Y_{\mathrm{ref2}}}, \quad g_2\left(\frac{t}{h}\right) = \frac{Y_{\mathrm{m}}^{\mathrm{n}}\left(\frac{b}{w} = 0.114, \frac{t}{h}\right)}{Y_{\mathrm{ref2}}}, \quad Y_{\mathrm{ref2}} = Y_{\mathrm{m}}^{\mathrm{n}}\left(\frac{b}{w} = 0.114, \frac{t}{h} = 0.2\right)$$

### 4.2. Results

#### 4.2.1. Validation of the H-integral approach

Before it can be conveniently applied to study the fracture problem, the accuracy of the H-integral should be quantified for the Si-Glass-Si triple stack problem. It is found that for the MESA and FRAME specimens, the stress intensity factors calculated from the H-integral agree very well with asymptotic solutions obtained directly by finite element computations of displacements along the notch flanks or of the stress along the interface. The variations are within 5% for all calculations.

Tables 1–4 ($Y_{\mathrm{ref}}$ in boldface) show the dimensionless stress intensity factors $Y_{\mathrm{I}}^{\mathrm{n}}$ and $Y_{\mathrm{II}}^{\mathrm{n}}$ obtained from H-integral and asymptotic analysis with different bond length and glass thickness for both MESA and FRAME specimens.

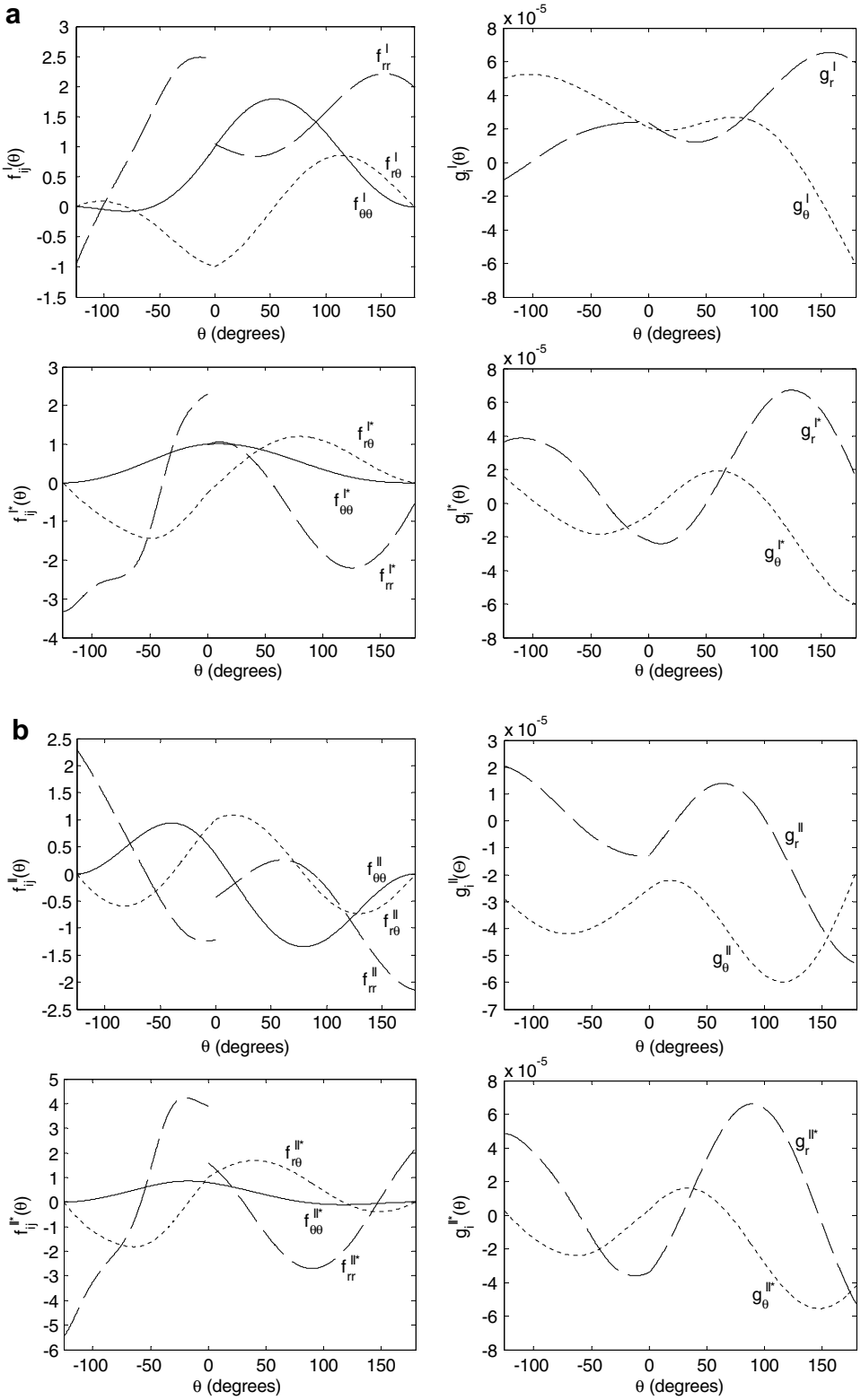


Fig. 3. Angular variation of the stress and displacement fields (a) $f_{ij}^{\mathrm{I}}(\theta)$, $g_i^{\mathrm{I}}(\theta)$, $f_{ij}^{\mathrm{I}^*}(\theta)$, $g_i^{\mathrm{I}^*}(\theta)$ and (b) $f_{ij}^{\mathrm{II}}(\theta)$, $g_i^{\mathrm{II}}(\theta)$, $f_{ij}^{\mathrm{II}^*}(\theta)$, $g_i^{\mathrm{II}^*}(\theta)$ for Si-Glass-Si triple stacks with notch angle $\gamma = 54.74°$.

Table 1
$Y_{\mathrm{I}}^{\mathrm{n}}$ and $Y_{\mathrm{II}}^{\mathrm{n}}$ obtained from H-integral and asymptotic analysis with $\frac{a}{w} = 0.286$ for MESA specimens

| $t/h$ | $Y^{\mathrm{I}}_{\text{H-integral}}$ | $Y^{\mathrm{I}}_{u\theta\text{-asymptotic}}$ | $Y^{\mathrm{I}}_{s\theta\theta\text{-asymptotic}}$ | $Y^{\mathrm{II}}_{\text{H-integral}}$ | $Y^{\mathrm{II}}_{u\theta\text{-asymptotic}}$ | $Y^{\mathrm{II}}_{s\theta\theta\text{-asymptotic}}$ |
|---|---|---|---|---|---|---|
| 0.167 | 0.477 | 0.461 | 0.488 | 0.986 | 0.942 | 0.972 |
| 0.200 | **0.479** | 0.464 | 0.488 | 0.978 | 0.937 | 0.966 |
| 0.278 | 0.483 | 0.469 | 0.489 | 0.964 | 0.928 | 0.955 |
| 0.556 | 0.491 | 0.479 | 0.492 | 0.935 | 0.910 | 0.932 |

Table 2
$Y_{\mathrm{I}}^{\mathrm{n}}$ and $Y_{\mathrm{II}}^{\mathrm{n}}$ obtained from H-integral and asymptotic analysis with $\frac{t}{h} = 0.2$ for MESA specimens

| $a/w$ | $Y^{\mathrm{I}}_{\text{H-integral}}$ | $Y^{\mathrm{I}}_{u\theta\text{-asymptotic}}$ | $Y^{\mathrm{I}}_{s\theta\theta\text{-asymptotic}}$ | $Y^{\mathrm{II}}_{\text{H-integral}}$ | $Y^{\mathrm{II}}_{u\theta\text{-asymptotic}}$ | $Y^{\mathrm{II}}_{s\theta\theta\text{-asymptotic}}$ |
|---|---|---|---|---|---|---|
| 0.200 | 0.579 | 0.561 | 0.589 | 1.177 | 1.128 | 1.163 |
| 0.286 | **0.479** | 0.464 | 0.488 | 0.978 | 0.937 | 0.966 |
| 0.404 | 0.394 | 0.381 | 0.401 | 0.806 | 0.776 | 0.797 |
| 0.486 | 0.350 | 0.339 | 0.357 | 0.719 | 0.695 | 0.711 |
| 0.571 | 0.311 | 0.302 | 0.317 | 0.640 | 0.612 | 0.633 |

Table 3
$Y_{\mathrm{I}}^{\mathrm{n}}$ and $Y_{\mathrm{II}}^{\mathrm{n}}$ obtained from H-integral and asymptotic analysis with $\frac{b}{w} = 0.114$ for FRAME specimens

| $t/h$ | $Y^{\mathrm{I}}_{\text{H-integral}}$ | $Y^{\mathrm{I}}_{u\theta\text{-asymptotic}}$ | $Y^{\mathrm{I}}_{s\theta\theta\text{-asymptotic}}$ | $Y^{\mathrm{II}}_{\text{H-integral}}$ | $Y^{\mathrm{II}}_{u\theta\text{-asymptotic}}$ | $Y^{\mathrm{II}}_{s\theta\theta\text{-asymptotic}}$ |
|---|---|---|---|---|---|---|
| 0.167 | 0.494 | 0.478 | 0.506 | 1.020 | 0.980 | 1.010 |
| 0.200 | **0.497** | 0.481 | 0.506 | 1.018 | 0.979 | 1.005 |
| 0.278 | 0.503 | 0.488 | 0.509 | 1.007 | 0.973 | 0.998 |
| 0.556 | 0.518 | 0.506 | 0.520 | 0.991 | 0.970 | 0.986 |
| 1.000 | 0.536 | 0.524 | 0.536 | 0.983 | 0.963 | 0.982 |

Table 4
$Y_{\mathrm{I}}^{\mathrm{n}}$ and $Y_{\mathrm{II}}^{\mathrm{n}}$ obtained from H-integral and asymptotic analysis with $\frac{t}{h} = 0.2$ for FRAME specimens

| $b/w$ | $Y^{\mathrm{I}}_{\text{H-integral}}$ | $Y^{\mathrm{I}}_{u\theta\text{-asymptotic}}$ | $Y^{\mathrm{I}}_{s\theta\theta\text{-asymptotic}}$ | $Y^{\mathrm{II}}_{\text{H-integral}}$ | $Y^{\mathrm{II}}_{u\theta\text{-asymptotic}}$ | $Y^{\mathrm{II}}_{s\theta\theta\text{-asymptotic}}$ |
|---|---|---|---|---|---|---|
| 0.114 | **0.497** | 0.481 | 0.506 | 1.018 | 0.979 | 1.005 |
| 0.229 | 0.335 | 0.325 | 0.341 | 0.693 | 0.668 | 0.685 |
| 0.343 | 0.275 | 0.266 | 0.280 | 0.571 | 0.546 | 0.564 |
| 0.457 | 0.246 | 0.238 | 0.250 | 0.511 | 0.492 | 0.505 |
| 0.543 | 0.234 | 0.227 | 0.238 | 0.486 | 0.466 | 0.480 |

### *4.2.2. Empirical solutions of $Y_{\mathrm{I}}^{\mathrm{n}}$ and $Y_{\mathrm{II}}^{\mathrm{n}}$ for MESA and FRAME specimens*

To facilitate engineering application, we established empirical solutions of $Y_{\mathrm{I}}^{\mathrm{n}}$ for MESA and FRAME specimens. The following geometrical ranges are considered: the solutions are applicable over the range $0.2 \leqslant \frac{a}{w} \leqslant 0.571, 0.167 \leqslant \frac{t}{h} \leqslant 0.556$ for MESA specimens, and over the range $0.114 \leqslant \frac{b}{w} \leqslant 0.543, 0.167 \leqslant \frac{t}{h} \leqslant 1$ for FRAME specimens, respectively. According to Eq. (4.3), the normalized results obtained from H-integral approach are accurately fitted by the power function $f_i(\text{geometry}) = j(\text{geometry})^k$ and $g_i(\text{geometry}) = l(\text{geometry})^s$, $i = 1, 2$. The best-fit values of the parameters $j, k, l$ and $s$ are shown in Figs. 4 and 5 for MESA and FRAME, respectively.

From Eqs. (4.2) and (4.3), the dimensionless stress intensity factor $Y_{\mathrm{I}}^{\mathrm{n}}$ obtained from the H-integral can be fitted by the following functions:

$$Y^{\mathrm{I}}_{\text{H-integral}}\left(\frac{a}{w}, \frac{t}{h}\right) = Y^{\mathrm{I}}_{\text{ref1}} \times 0.39848\left(\frac{a}{w}\right)^{-0.57552} \times 1.03873\left(\frac{t}{h}\right)^{0.02355} \tag{4.4}$$

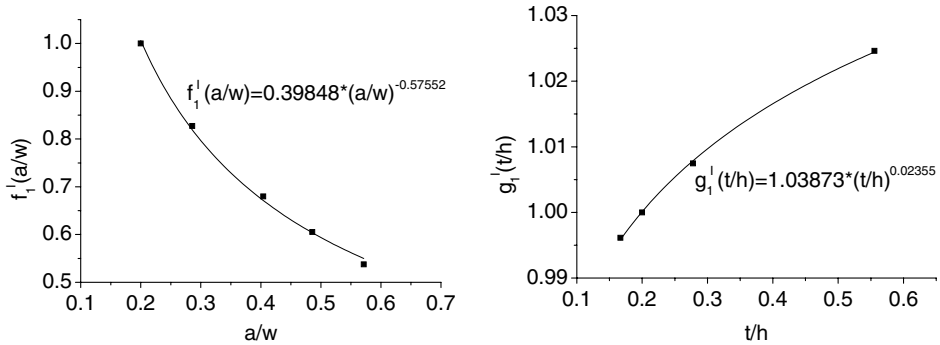


Fig. 4. $f_1^{\mathrm{I}}\left(\frac{a}{w}\right)$ and $g_1^{\mathrm{I}}\left(\frac{t}{h}\right)$ for MESA specimens $\left(0.2 \leqslant \frac{a}{w} \leqslant 0.571, 0.167 \leqslant \frac{t}{h} \leqslant 0.556\right)$.

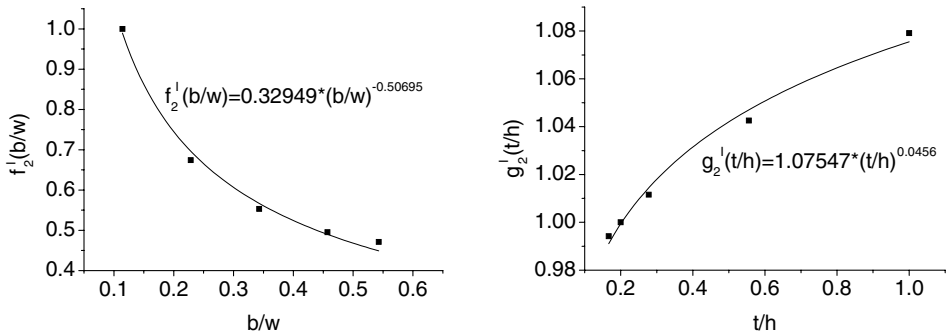


Fig. 5. $f_2^{\mathrm{I}}\left(\frac{b}{w}\right)$ and $g_2^{\mathrm{I}}\left(\frac{t}{h}\right)$ for FRAME specimens $\left(0.114 \leqslant \frac{b}{w} \leqslant 0.543, 0.167 \leqslant \frac{t}{h} \leqslant 1\right)$.

where

$$Y_{\mathrm{ref1}}^{\mathrm{I}} = Y_{\left(\frac{a}{w}=0.286, \frac{t}{h}=0.2\right)}^{\mathrm{I}} = 0.479 \quad \text{and} \quad 0.2 \leqslant \frac{a}{w} \leqslant 0.571, \quad 0.167 \leqslant \frac{t}{h} \leqslant 0.556.$$

for the MESA specimens, and

$$Y_{\text{H-integral}}^{\mathrm{I}}\left(\frac{b}{w}, \frac{t}{h}\right) = Y_{\mathrm{ref2}}^{\mathrm{I}} \times 0.32949\left(\frac{b}{w}\right)^{-0.50695} \times 1.07547\left(\frac{t}{h}\right)^{0.0456} \tag{4.5}$$

where

$$Y_{\mathrm{ref2}}^{\mathrm{I}} = Y_{\left(\frac{b}{w}=0.114, \frac{t}{h}=0.2\right)}^{\mathrm{I}} = 0.497 \quad \text{and} \quad 0.114 \leqslant \frac{b}{w} \leqslant 0.543, \quad 0.167 \leqslant \frac{t}{h} \leqslant 1.$$

for the FRAME specimens.

Fig. 6 compares the $Y_{\text{H-integral}}^{\mathrm{I}}$ and $Y_{\text{H-integral}}^{\mathrm{II}}$. It can be observed from Fig. 6 that both $Y_{\text{H-integral}}^{\mathrm{I}}$ and $Y_{\text{H-integral}}^{\mathrm{II}}$ decrease with increasing bond area.

### 4.2.3. Effect of glass thickness

In order to understand the effect of glass thickness on the stress intensity factor, we have artificially extended glass thickness to $t = 1750$ μm. Fig. 7 compares the thin-film MESA specimen with glass thickness $t = 3$ μm and the extreme bimaterial MESA specimen with glass thickness $t = 1750$ μm. It can be observed that the thicker the glass layer, the higher the $Y_{\text{H-integral}}^{\mathrm{I}}$.

It also has been found from Fig. 8 that the $Y_{\mathrm{I}}^{\mathrm{n}}$ increases with glass thickness while basically decreases for mode II loading as the glass thickness increases. Furthermore, for thin-film MESA and FRAME specimens, Fig. 9, it can be observed that varying thickness of glass does not affect $Y_{\mathrm{I}}^{\mathrm{n}}$ and $Y_{\mathrm{II}}^{\mathrm{n}}$ significantly. Nevertheless,

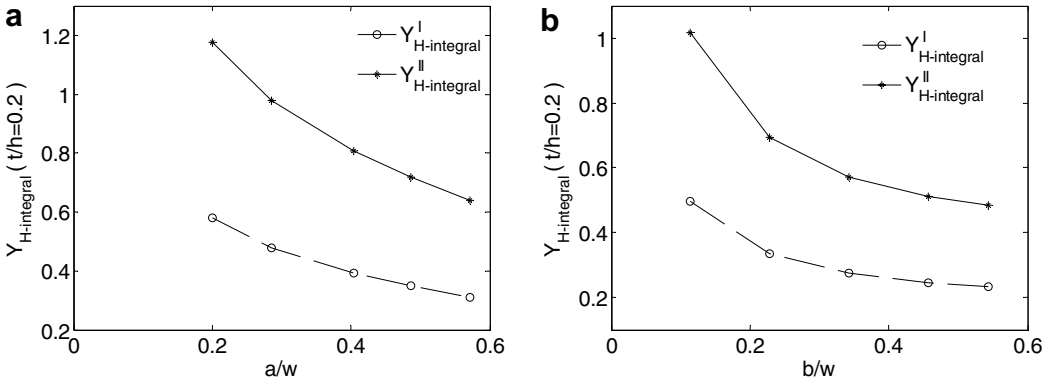


Fig. 6. $Y^{I}_{H\text{-integral}}$ and $Y^{II}_{H\text{-integral}}$ for (a) MESA specimens and (b) FRAME specimens.

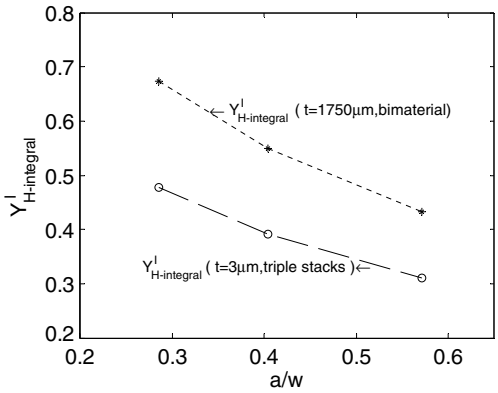


Fig. 7. The dimensionless stress intensity factors for two glass thicknesses.

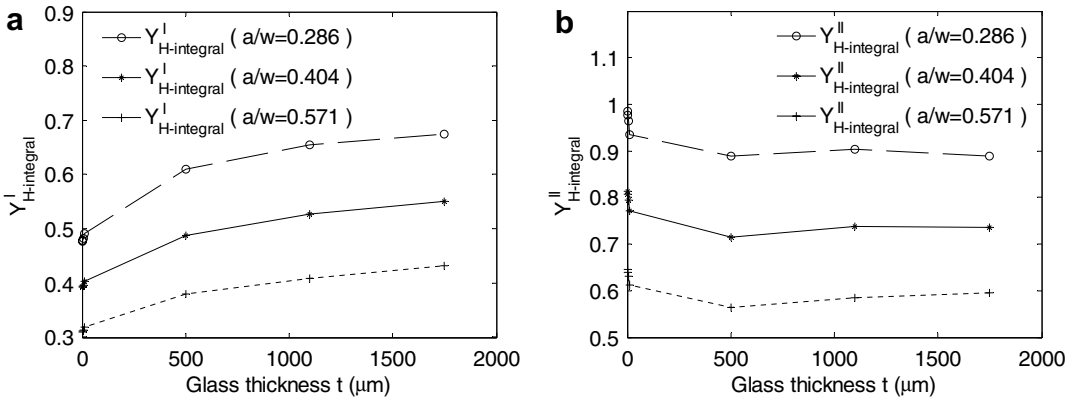


Fig. 8. (a) $Y^{I}_{H\text{-integral}}$ and (b) $Y^{II}_{H\text{-integral}}$ for MESA specimens with glass thickness over the range 3–1750 μm.

for the other MESA specimens with thicker glass layer, the stress intensity factors differ greatly. Hence, it can be concluded that the glass thickness is an important geometrical quantity affecting the stress intensity factors for triple stacks with thick glass layer.

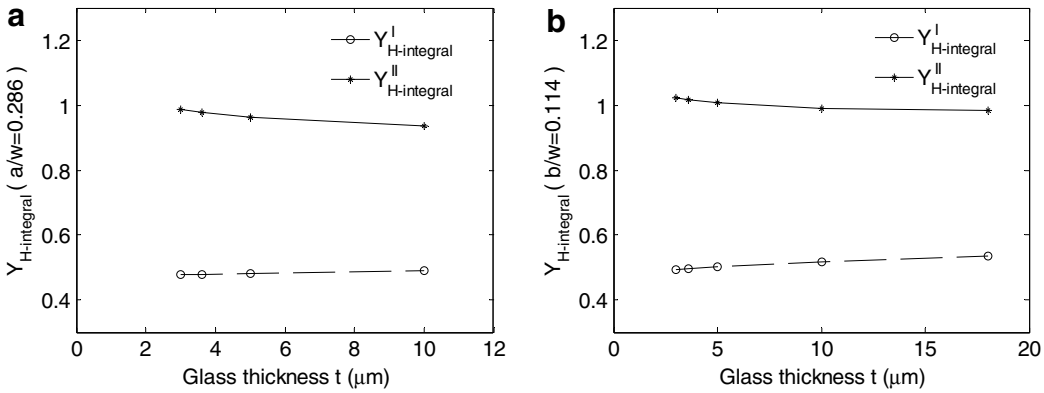


Fig. 9. $Y^{I}_{H\text{-integral}}$ and $Y^{II}_{H\text{-integral}}$ for thin-film (a) MESA and (b) FRAME triple stacks.

### 4.2.4. Failure criterion

Fracture resistance of structural components with stress concentration at sharp notches can be evaluated by different failure criteria. As discussed earlier, the notch tip in both MESA and FRAME specimens is subjected to mixed-mode loading. It is interesting to investigate the failure criterion. In order to assess whether $K^{n}_{IC}$ can be used to predict fracture initiation, various MESA and FRAME specimens were designed for pull tests [3]. Ten to twenty different test specimens were used for each specific bond area and the experimental failure strength was fitted to Weibull distributions. Chips were glued onto grinded hexagonal head cap screws with a thin layer of Micro Bond™ III CTCA3-3 or Loctite 420. The dimensions of the test specimen are summarized in Table 5. One wafer in each wafer couple for thin-film anodic bonding experiment was covered with a sputtered layer of PYREX, Corning#7740 glass ($3.6 \pm 0.2$ μm thick) on top of a thin dielectric layer. A thin dielectric layer was always grown or deposited before sputtering of the glass layer so as to reduce the possibility of electrical breakdown during the bonding process. The thin dielectric layer was removed from the backside of the wafers before bonding for electrical contacting.

It is well known that a traditional yield criterion is not applicable to correlate with failure because typically the failure load measured from tests depends on specimen geometry, size and type of remote loading. Instead, some studies have shown that the critical stress intensity factor $K^{n}_{C}$ can be used as a single parameter to correlate fracture initiation at sharp notches, which is possibly independent of some geometry parameters [10,18,22,28].

The corner in the present test specimens involves mixed-mode deformation. From the asymptotic analysis, the stress singularity for mode I is strong, but it is weaker for mode II. This is discussed by Dunn et al. [18]. In this case, the critical stress intensity $K^{n}_{C} = \{K^{n}_{IC}, K^{n}_{IIC}\}$ is mainly characterized by $K^{n}_{IC}$. The critical notch stress intensity factor, $K^{n}_{IC}$, can be computed from Eq. (4.2) using $\sigma_0 = \sigma_f$, the nominal failure strength, which is calculated using the measured failure force divided by the overall structure cross-section area in the pull test. According to average fracture strength $\sigma_f$ [3], the critical stress intensity factors $K^{n}_{IC}$ based on the test specimens are shown in Fig. 10. For the MESA specimen, the critical stress intensity factor $K^{n}_{IC}$ obtained for the averaged failure strength for the three specimens of different bond length are 1.01, 1.26 and

Table 5
Dimensions of bond areas for test specimens for pull tests [3]

| Geometry name | Outer dimensions (μm × μm) | Inner dimensions (μm × μm) |
|---|---|---|
| MESA 1 | 1000 × 1000 | – |
| MESA 2 | 1414 × 1414 | – |
| MESA 3 | 2000 × 2000 | – |
| FRAME 1 | 2700 × 2700 | 2300 × 2300 |
| FRAME 2 | 2700 × 2700 | 1900 × 1900 |
| FRAME 3 | 2700 × 2700 | 1100 × 1100 |
| **Etch process** | 500 g KOH:1 l DIW, 80 °C, 18–20 μm | |

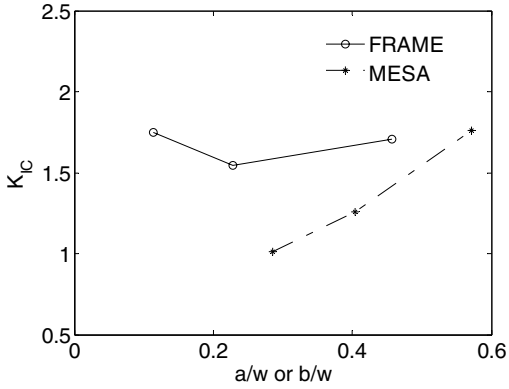


Fig. 10. The critical stress intensity factor for MESA and FRAME specimens.

Table 6
Comparison of the experimental and predicted nominal failure strength $\sigma_f$

| Specimen | Weibull average experimental $\sigma_f$ (MPa) | Predicted $\sigma_f$ (MPa) | Specimen | Weibull average experimental $\sigma_f$ (MPa) | Predicted $\sigma_f$ (MPa) |
|---|---|---|---|---|---|
| MESA1 | 1.600 | 2.126 | FRAME 1 | 2.674 | 2.545 |
| MESA2 | 2.424 | 2.587 | FRAME 2 | 3.497 | 3.775 |
| MESA3 | 4.286 | 3.271 | FRAME 3 | 5.257 | 5.139 |

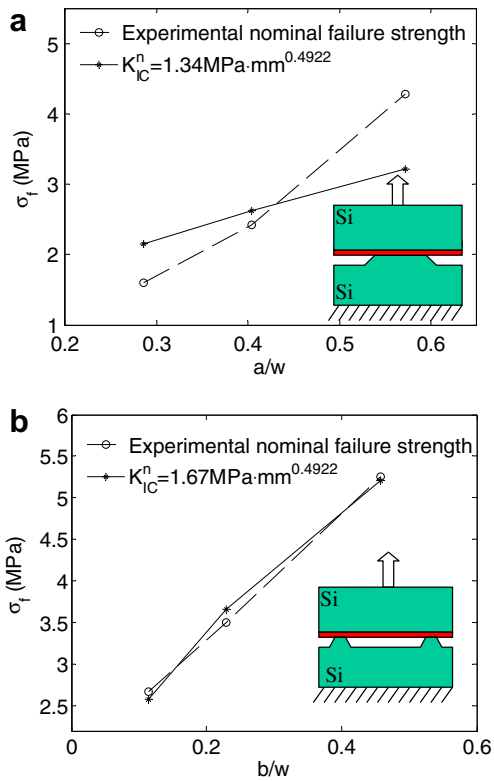


Fig. 11. The experimental and predicted nominal failure strength $\sigma_f$ for (a) MESA and (b) FRAME.

1.76 MPa mm$^{0.4922}$, respectively; while for the FRAME, the corresponding critical stress intensity factors are 1.75, 1.54 and 1.71 MPa m$^{0.4922}$. The average value of $K_{IC}^{n}$ is 1.34 MPa mm$^{0.4922}$ for MESA specimens and 1.67 MPa mm$^{0.4922}$ for FRAME specimens, respectively. The averaged experimental nominal failure strengths

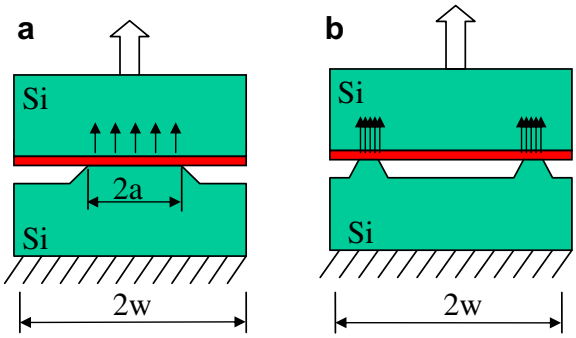


Fig. 12. Schematic definition of net-section bond strength $\sigma_N$ for (a) MESA and (b) FRAME.

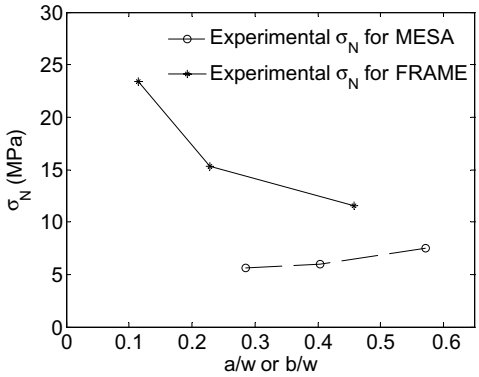


Fig. 13. Net-section bond strength $\sigma_N$ for MESA and FRAME specimens.

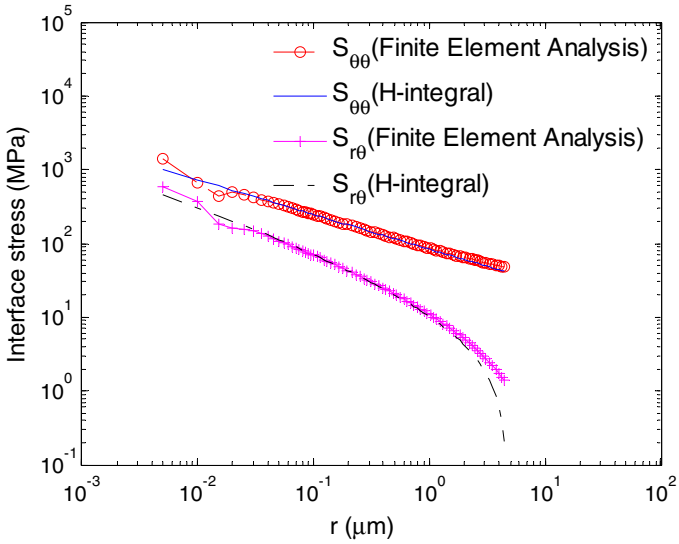


Fig. 14. Interface stress near the notch tip with $\frac{b}{w} = 0.229$ and $\frac{t}{h} = 0.2$ for FRAME specimens.

and the strengths calculated using the averaged $K_{IC}^{n}$ for the different bond area are shown in Table 6 and Fig. 11. It can be seen that the averaged $K_{IC}^{n}$ can be used to predict brittle fracture of the anodic-bonded FRAME specimens. However, for the MESA specimens the agreement is not very satisfactory. The cause of deviations for MESA specimens will be studied subsequently in more detail (Section 5.2).

It should be noted that the failure strength employed in the industry is defined as the measured failure force divided by the overall bonded area, i.e., the net-section bond strength $\sigma_N$ (see Fig. 12). The bond strength for MESA and FRAME specimens are shown in Fig. 13. It can be seen from Fig. 13 that a distinct geometry dependence is not observed for MESA specimens, but for FRAME specimens a significant geometry effect can be seen. With respect to the bond area, a large bond strength of the thinnest FRAME was observed, but increasing the bond area for the FRAME specimen does not necessarily lead to a proportionally higher resistance against an externally applied force.

The failure criterion applied here is based on the assumption that K-dominated annulus exists around the interface corner. The elastic fields can neither be very close to notch tip which is disturbed by material non-linearities and geometric irregularities nor be far away from the interface corner which is affected by far-field loading and boundaries. To qualify this K-dominated annulus, finite element analysis is performed at failure loads. The accuracy of the failure criterion is further depicted in Fig. 14 which shows a logarithmic diagram of the interface normal and shear stresses near the notch tip with $\frac{b}{w} = 0.229$ and $\frac{t}{h} = 0.2$. The normal stress $\sigma_{\theta\theta}$ obtained from two methods agrees to 5% within a distance of 2.5 μm while the shear stress $\sigma_{r\theta}$ agrees to 10% within a distance of 0.7 μm. Similar results are obtained for other specimens.

## 5. Discussion

### 5.1. Mesh effect

The important feature of H-integral approach is that a relatively coarse mesh can be used for the finite element analysis [22,29]. For example, for MESA specimen with $\frac{a}{w} = 0.286$ and $\frac{t}{h} = 0.278$, a fine and coarse mesh near the notch tip are depicted in Fig. 15. Through the glass layer, only five elements are created for the coarse mesh model while 39 elements are used for the fine mesh model. The smallest element size for the fine and coarse mesh is 0.01 and 1 μm, respectively. It should be pointed out that the smallest mesh size is restricted by geometric conditions around the notch tip, such as glass thickness, etching depth and so on. Furthermore, four integral contours around the notch tip are tested with the coarse meshes and the values of mode I stress intensity factors are 2.154, 2.137, 2.155, and 2.145 MPa mm$^{0.4922}$, respectively. As a result, the deviation of stress intensity from 2.137 MPa mm$^{0.4922}$ obtained from fine mesh is less than 1%.

### 5.2. Uncertainties

In this section, we further interpret the reasons resulting in deviation for MESA specimens and discuss the applicability of a critical stress intensity factor.

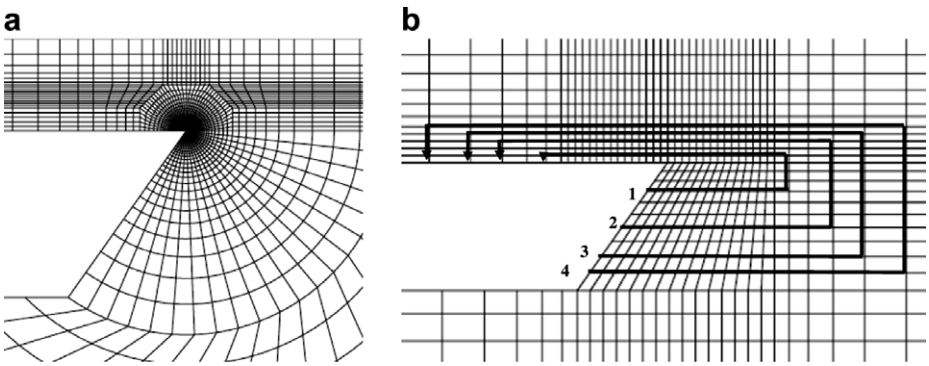


Fig. 15. (a) Fine mesh and (b) coarse mesh at a close look near the notch tip For MESA Specimen with $\frac{a}{w} = 0.286$ and $\frac{t}{h} = 0.278$.

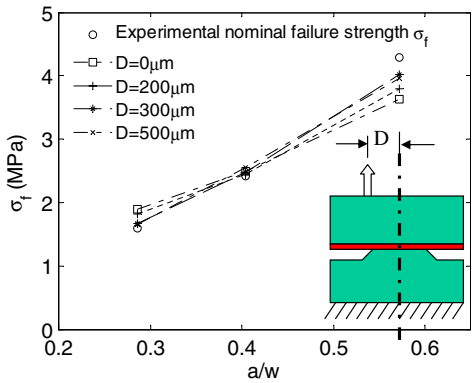


Fig. 16. The effect of loading misalignment on the predicted nominal failure strength $\sigma_f$.

For the MESA specimens, the predicted nominal failure strength did not match very well with experimental values. We believe this is mainly due to the difficult control of the loading alignment. The effect of misalignment has been further studied, Fig. 16. Several misalignment values have been tried. It has been found that a loading misalignment of $D = 300$ μm will result in a much better agreement. The FRAME specimens are less sensitive to loading misalignment due to large redundancy.

An important issue for notch mechanics is to understand the applicability of the critical stress intensity factor $K_{IC}^{n}$ for interface corners. Actually, $K_{IC}^{n}$ can no longer be simply treated as a size-independent material parameter like that in the linear elastic fracture mechanics. It depends not only on interface corner geometry and material elastic constants, but also on interface strength resulting in diverse failure modes. For instance, Dunn et al. [18] and Labossiere et al. [30] carried out similar tests with a weaker interface and obtained smaller critical stress intensity factor than that with a strong interface. For the test specimens employed herein, we have a strongly bonded interface and it was also observed that fracture initiated from the notch tip and propagated into the glass or partly along the bonded interface.

In addition, residual stress can possibly influence the results and it deserves attention in the future work. It may be one of the reasons for the scatter of failure strength in the tests.

Furthermore, it is observed from finite element analyses that the thickness of Si-wafers also affects the dimensionless stress intensity factor. For thin Si-wafers, for example, 0.35–1.75 mm thick, the values of mode I stress intensity can apparently vary with thickness of Si-wafers. However, when Si-wafers are thick enough, for instance, larger than 1.75 mm, the thickness dependence will disappear. This effect will be investigated more in the future.

Finally, the critical stress intensity factor $K_{IC}^{n}$ derived here did not yield the same value for both MESA and FRAME specimens with the same notch angle. The exact reasons are not apparent. Apart from the discussions above, the possible reasons leading to the differences are as follows: the simplified use of a single parameter $K_{IC}^{n}$ in mixed-mode loading, the control of loading alignment, different failure modes and the effect of residual stress.

## 6. Conclusions

For the triple stacks interface corner problem considered in this paper, the stress intensity factors obtained from the H-integral approach show excellent agreement with those obtained from the asymptotic solutions by finite element calculations of displacements along the notch flanks or of stresses along the interface. The deviation of the displacement approach and the stress approach from the H-integral approach is less than 5%.

The effect of glass thickness on the stress intensity factor has been studied. It has been found that the mode I stress intensity factor increases with glass thickness while basically decreases for mode II loading as the glass thickness increases. Moreover, the stress intensity factors vary significantly with a thicker glass layer but are not affected greatly for thin-film anodic-bonded triple stacks. Hence, it turns out that the glass thickness is an important geometrical quantity affecting the stress intensity factors for triple stacks with a thick glass layer.

In order to facilitate engineering application, empirical solutions of stress intensity factors for MESA and FRAME specimens have been proposed. It should be pointed out that the critical stress intensity factor $K_{IC}^{n}$ depends on the interface corner geometry, material elastic constants, failure modes and residual stress. In this paper, $K_{IC}^{n} = 1.34\ \text{MPa mm}^{0.4922}$ and $K_{IC}^{n} = 1.67\text{MPa mm}^{0.4922}$ have been used to characterize MESA and FRAME specimens, respectively. Loading alignment has been found to play a significant role in fracture behavior of MESA specimens.

## References


[1] Wallis G, Pomerantz DI. Field assisted glass-metal sealing. J Appl Phys 1969;40:3946–9.
[2] Brooks AD, Donovan RP. Low-temperature electrostatic silicon-to-silicon seals using sputtered borosilicate glass. J Electrochem Soc 1972;119(4):545–6.
[3] Visser MM. Wafer bonding for MEMS, PhD thesis, University of Oslo, 2002.
[4] Quenzer HJ, Schulz AV, Kinkopf T, Helm T. Anodic-bonding on glass layers prepared by a spin-on glass process: preparation process and experimental results. In: Transducers'01, Eurosensors XV (The 11th international conference on Solid-state Sensors and Actuators, Germany) 2001. p. 230–3.
[5] Choi WB, Ju BK, Lee YH, Jeong JW, Haskard MR, Lee NY, et al. Experimental analysis on the anodic bonding with an evaporated glass layer. J Micromech Microeng 1997;7:316–22.
[6] Williams ML. Stress singularities resulting from various boundary conditions in angular corners of plates in extension. J Appl Mech 1952;19:526–8.
[7] Bogy DB, Wang KC. Stress singularities at interface corners in bonded dissimilar isotropic elastic materials. Int J Solids Struct 1971;7:993–1005.
[8] Dempsey JP, Sinclair GB. On the stress singularities in the plane elasticity of the composite wedge. J Elast 1979;9:373–91.
[9] Dunn ML, Suwito W, Cunningham S, May CW. Fracture initiation at sharp notches under mode I, mode II, and mild mixed-mode loading. Int J Fract 1997;84:367–81.
[10] Dunn ML, Suwito W, Cunningham S. Fracture initiation at sharp notches: correlation using critical stress intensity. Int J Solids Struct 1997;34:3873–83.
[11] Dempsey JP, Sinclair GB. On the singular behavior at the vertex of a bimaterial wedge. J Elast 1981;11:317–27.
[12] Hein VL, Erdogan F. Stress singularities in a two material wedge. Int J Fract Mech 1971;7:317–30.
[13] Cho SB, Lee KR, Choy YS, Yuuki R. Determination of stress intensity factors and boundary element analysis for interface cracks in dissimilar anisotropic materials. Engng Fract Mech 1992;43(4):603–14.
[14] Pageau SS, Joseph PF, Biggers SB. Finite element analysis of anisotropic materials with singular inplane stress fields. Int J Solids Struct 1995;32:571–91.
[15] Suwito W, Dunn ML, Cunningham SJ, Read DT. Elastic moduli, strength, and fracture initiation at sharp notches in etched single crystal silicon microstructures. J Appl Phys 1999;85(7):3519–34.
[16] Suwito W, Dunn ML, Cunningham SJ. Fracture Initiation at Sharp Notches in single crystal silicon. J Appl Phys 1998;83:3574–82.
[17] Wu KC, Chen CT. Stress analysis of anisotropic elastic V-notched bodies. Int J Solids Struct 1996;33(17):2403–16.
[18] Dunn ML, Cunningham SJ, Labossire PEW. Initiation toughness of silicon/glass anodic bonds. Acta Mater 2000;48:735–44.
[19] Ting TCT. Stress singularities at the tip of interfaces in polycrystals. In: Rossmanith, editor. Damage and failure of interfaces. Rotterdam: Balkema; 1998. p. 75–82.
[20] Ting TCT, Chou SC. Edge singularities in anisotropic composites. Int J Compos Struct 1981;17(11):1057–68.
[21] Hutchinson JW, Suo Z. Mixed mode cracking in layered materials. Adv Appl Mech 1992;29:63–191.
[22] Labossiere PEW, Dunn ML. Stress intensities at interface corners in anisotropic bimaterials. Engng Fract Mech 1999;62:555–75.
[23] Stroh AN. Dislocations and cracks in anisotropic elasticity. Phil Mag 1958;3:625–46.
[24] Ting TCT. Anisotropic elasticity: theory and applications. Oxford University Press; 1996.
[25] Eshelby JD, Read WT, Shockley W. Anisotropic elasticity with applications to dislocation theory. Acta Metall 1953;1:251–9.
[26] Mason WP. Physical acoustics and properties of solids. New York: Van Nostrand; 1958.
[27] Wu KC, Chang FT. Near-tip fields in a notched body with dislocations and body forces. ASME J Appl Mech 1993;60:936–41.
[28] Suwito W. Fracture of notched silicon microstructures, PhD thesis, University of Colorado, 1997.
[29] Zhang ZL, Mikkola TPJ. A simple path-independent integral for calculating mixed-mode stress intensity factors. Fatigue Fract Engng Mater Struct 1992;15(10):1041–9.
[30] Labossiere PEW, Dunn ML, Cunningham SJ. Application of biomaterial interface corner failure mechanics to silicon/glass anodic bonds. J Mech Phys Solids 2002;50:405–33.